

Noname manuscript No.
(will be inserted by the editor)

**1 Local wind regime induced by the presence of giant
2 linear dunes.**

**3 Cyril Gadal · Pauline Delorme ·
4 Clément Narteau · Giles Wiggs ·
5 Matthew Baddock · Joanna M. Nield ·
6 Philippe Claudin**

7
8 Received: DD Month YEAR / Accepted: DD Month YEAR

9 Abstract

10 Keywords Boundary layer · Turbulent flow · Sand dunes · Fluide-structures
11 interactions

C. Gadal

Institut de Mécanique des Fluides de Toulouse (IMFT), Université de Toulouse, CNRS,
INPT, UPS, Toulouse, France
E-mail: cyril.gadal@imft.fr

S. Author
second address

T. Author
third address

12 1 Introduction

13 As a flow encounters an obstacle, different interactions can arise depending on
14 the different time and length scales involved. In the case of atmospheric flows,
15 this mainly depends on the part of the atmosphere, schematically composed of
16 a turbulent boundary layer topped by a stably stratified one, with which the
17 obstacle interacts (Stull 1988). At the largest scale, the feedback of mountains
18 on the stratified part results in wave generation as well as significant wind
19 disturbances, such as downslope winds in the lee side (Durran 1990). Inside
20 the boundary layer, the interaction between a turbulent flow and hilly surfaces
21 is for example key to the understanding ocean surface wind-driven waves (Sul-
22 livan and McWilliams 2010), or eolian bedforms in desert (Courrech du Pont
23 2015).

24 Looking at the flow close to the surface, two different components of the
25 topography feedback can be isolated. First, the flow accelerates on the upwind
26 slope, and slows down on the downwind one, with a maximum velocity slightly
27 upwind of the crest (Jackson and Hunt 1975; Sykes 1980; Hunt et al. 1988).
28 Several measurements are available, performed in subaqueous flumes (Zilker
29 et al. 1977; Zilker and Hanratty 1979; Frederick and Hanratty 1988) and in
30 eolian field conditions (Claudin et al. 2013; Lü et al. 2021). Second, deflection
31 occurs when the incident flow direction is not perpendicular to the ridge crest.
32 While predicted to be small (less than 10°) in the linear regime (Gadal et al.
33 2019), significant flow steering has been reported in the field on the downwind
34 side of larger aspect ratios obstacles, such as mountain ranges (Kim et al. 2000;
35 Lewis et al. 2008; Fernando et al. 2019) or sand dunes (Walker et al. 2009;
36 Walker and Shugar 2013; Hesp et al. 2015; Smith et al. 2017).

37 In the case of aeolian bedforms, the measurements mentioned above were
38 made on dunes a few meters high only. The resulting wind disturbances have
39 then been shown to significantly impact the sediment pathways of the system
40 (Hesp et al. 2015), but also to affect the collective behaviour of dune pop-
41ulations trough long-range interactions (Bacik et al. 2020). However, eolian
42 dunes coexists in sand seas at different scales, each representative of their
43 different evolution stages, from emergence at twenty meters wavelengths to gi-
44 ant size, corresponding to kilometric wavelengths and heights of several dozen
45 meters (McKee 1979). Quantifying these two effects for giant dunes is then
46 all the more important for several reasons. First, larger wind disturbances
47 are expected from larger obstacles. Second, the flow-structure coupling is
48 not straightforward due to vertical structure of the atmosphere with which
49 the giant dunes interact due to their sizes (Andreotti et al. 2009). Finally,
50 the morphodynamics of aeolian bedforms are strongly dependent on the wind
51 regime (Livingstone and Warren 1996). Thus, small-scale bedforms are sen-
52sitive to wind disturbances induced by larger-scale bedforms. This has been
53 demonstrated for impact ripples on dunes (Howard 1977; Hood et al. 2021),
54 but has never been studied for medium-scale dunes near giant dunes.

55 In the literature, arid areas have been studied at the desert scale from
56 climate reanalyses based on global atmospheric models (Blumberg and Greeley

57 1996; Livingstone et al. 2010; Ashkenazy et al. 2012; Jolivet et al. 2021; Hu
58 et al. 2021), such as ERA-40, ERA-Interim or ERA-5 (Uppala et al. 2005;
59 Dee et al. 2011; Hersbach et al. 2020). However, the spatial resolution (tens of
60 kilometers) of these reanalyses implies average quantities that do not resolve
61 the smaller scales, ranging from the study of individual dunes to the border of
62 mountains (Livingstone et al. 2010). Lately, the release of ERA5-Land allow to
63 push back this limitation by providing up to 70 years of hourly wind predictions
64 at a 9 km spatial resolution (Muñoz-Sabater et al. 2021). However, due to its
65 recent nature, the applicability limitations of this dataset remain to be studied.

66 Here, we compare local wind speeds and directions measured in four dif-
67 ferent places across the Namib desert to the regional predictions of the ERA5-
68 Land climate reanalysis. When the measurement stations are surrounded by a
69 relatively flat environment, we show that local measurements and regional pre-
70 dictions agree with each other. On the contrary, in the sand sea, we show that
71 they differ due to the presence of giant dunes. Furthermore, we link the magni-
72 tude of these discrepancies to the circadian cycle of the atmospheric boundary
73 layer. Finally, we draw implications for smaller-scale eolian bedforms.

74 **2 Wind regimes across the Namib Sand Sea**

75 We focus on four places across and nearby the Namib desert, highlighting
76 different environments (see Fig. 1). The Adamax station is located near the
77 Adamax salt pan, in a highly vegetated area. The Huab station, on the coast
78 at the outlet of the Huab river, is in an arid environment exhibiting 60-m scale
79 barchan dunes. While the surroundings of these two stations are relatively flat,
80 this is not the case for the Deep Sea and South Namib stations. Both are in
81 the interdune between tens of meters high giant linear dunes with kilomet-
82 ric wavelengths and superimposed patterns. In this section, we describe and
83 compare winds from local measurements and climate reanalysis predictions.

84 **2.1 Datasets**

85 Local winds are provided by measurement stations located in the four different
86 places (see black dots in Fig. 1). The wind strength and direction are sampled
87 every 10 minutes by cup anemometers and wind vanes, at heights between
88 2 m and 3 m depending on the station. The available period of measurements
89 ranges from 1 to 5 discontinuous years distributed between 2012 and 2020 (see
90 Fig. S1). We checked that at least one complete seasonal cycle is available at
91 each station. Regional winds are extracted at the same locations and periods
92 from the ERA5-Land dataset, which is a replay at a smaller spatial resolution
93 of ERA5, the latest climate reanalysis from the ECMWF (Hersbach et al.
94 2020; Muñoz-Sabater et al. 2021). It provides hourly predictions of the 10-m
95 wind velocity and direction at a spatial resolution of ~ 9 km ($0.1^\circ \times 0.1^\circ$).

96 For comparison, the local measurements are averaged into 1-hr bins cen-
97 tered on the temporal scale of the ERA5-Land estimates (see Fig. S2). As the

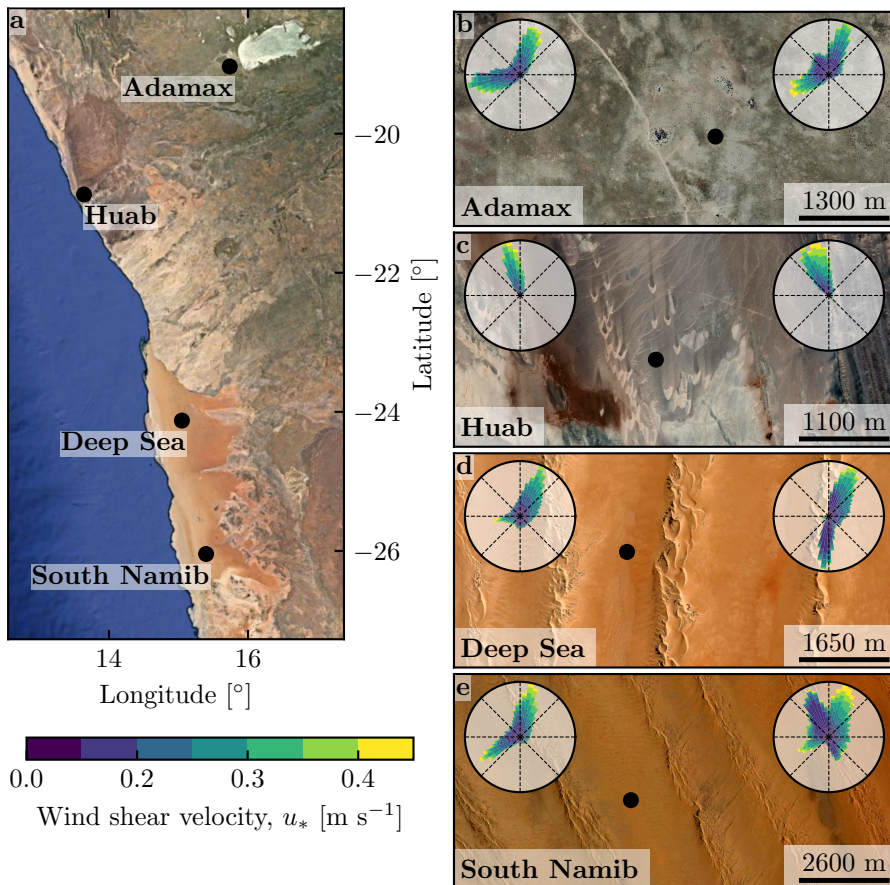


Fig. 1 Wind data used in this study **a**: Location of the studied sites. **b–e**: Satellite images of the studied sites (Google-Earth, Maxar Technologies, CNES/Airbus). In each subplot, the left and right wind roses represent the data from the ERA5Land climate reanalysis and the local wind stations, respectively. Note that the bars show the direction towards which the wind blows. The black dots show the location of local wind stations.

98 wind velocities of both datasets are provided at different heights, we convert
 99 them into shear velocities (see SI section 1), characteristic of the turbulent
 100 wind profile, which are then used together with the wind direction for further
 101 analysis. The resulting wind data are shown on the wind roses of Fig. 1(b–e).

102 Finally, the dune properties are computed using autocorrelation on the 30-
 103 m Digital Elevation Models (DEMs) of the shuttle radar topography mission
 104 (Farr et al. 2007). For the South Namib and Deep Sea stations, we obtain
 105 respectively orientations of 85° and 125° , wavelengths of 2.6 km and 2.3 km
 106 and amplitudes of 45 m and 20 m (see Fig. S4 for more details).

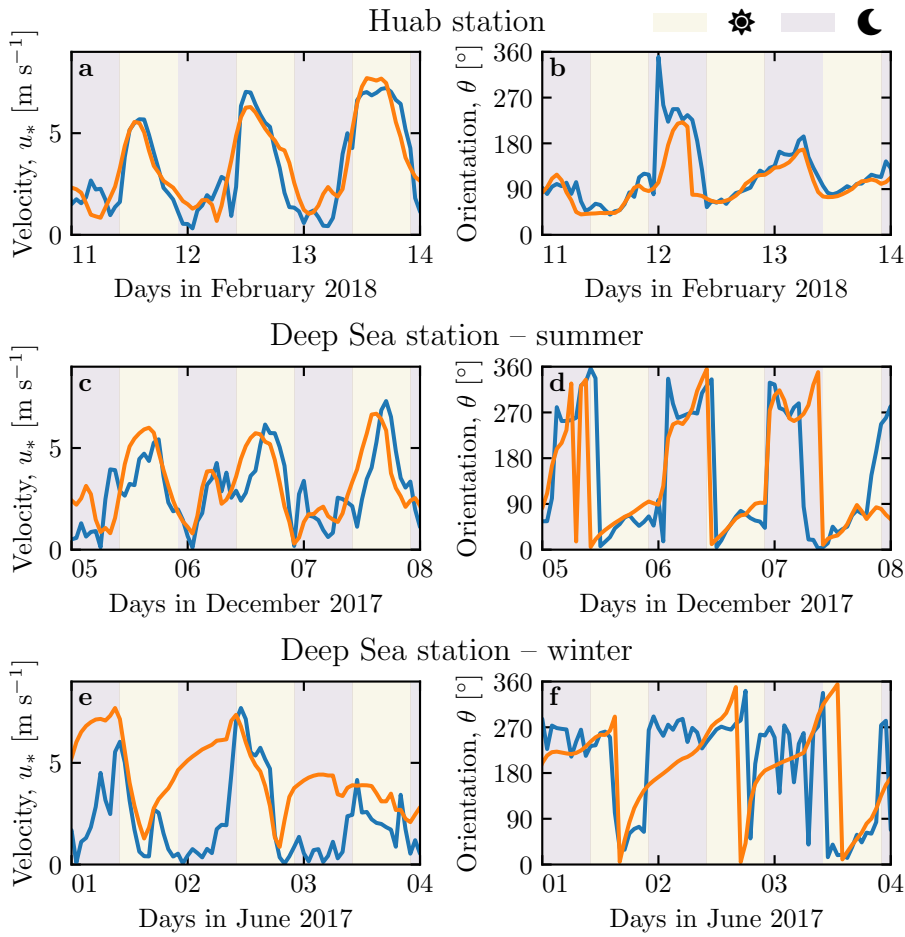


Fig. 2 Temporal comparison between the wind data coming from the Era5Land climate reanalysis (orange lines) and from the local measurements (blue lines). Color swatches indicate day (between 1000 UTC and 2200 UTC) and night (before 1000 UTC or after 2200 UTC). **a–b:** Huab station. **c–d:** Deep Sea station in winter. **e–f:** Deep Sea station in summer.

107 2.2 Agreement between local and regional winds

108 The obtained wind regimes are shown in figure 1. In the Namib, the regional
 109 wind patterns are essentially controlled by the see breeze, resulting in strong
 110 northward components (sometimes slightly deviated by the large scale topog-
 111 raphy) present in all regional wind roses (Lancaster 1985). These daytime
 112 winds are dominant during the second-half of the year (Septembre–January).
 113 In winter, an additional easterly component can be recorded during the night,
 114 induced by the combination of katabatic winds forming on the mountains,
 115 and infrequent ‘berg’ winds, which are responsible of the high wind velocities
 116 observed (Lancaster 1984). The frequency of these easterly components de-

117 creases from the inland to the coast, resulting in bidirectional wind regimes
 118 within the Namib Sand Sea and at the Adamax salt pan (Fig. 1b, 1d and 1e)
 119 and a unidirectional wind regime on the coast at the outlet of the Huab River
 120 (Fig. 1c).

121 In the case of the Adamax and Huab stations, the wind roses from the
 122 regional predictions qualitatively match those corresponding to the local mea-
 123 surements. However, for the Deep Sea and South Namib stations, the mea-
 124 sured wind roses exhibit additional components aligned with the giant dune
 125 orientation visible on the satellite images (Fig. 1c–d). The time series of wind
 126 speed and direction show that this agreement in the case of Adamax and Huab
 127 stations is always verified (Fig. 2a–b) and Fig. S5). In contrast, for the sta-
 128 tions within the giant dune field, we observe that this agreement is limited to
 129 Septembre–January time periods (Fig. 2c–d).

130 2.3 Influence of the giant dunes on local wind regimes

131 In the February–August period, when giant dunes are present, the local and re-
 132 gional winds match during daytime only, i.e when the southerly/southwesterly
 133 sea breeze dominates (see Fig. 2(e–f), Fig. 3 and Fig. S6). In the late after-
 134 noon and during the night, when the northwesterly ‘berg’ and katabatic winds
 135 blow, measurements and predictions differ. In this case, the angular wind dis-
 136 tribution of the local measurements exhibits two additional modes separated
 137 of $\simeq 180^\circ$, each corresponding to the giant dune alignment (see the purple
 138 frame in Fig. 3 and Fig. S6, as well as Fig. S7). This deviation is also associ-
 139 ated with a global attenuation of the wind strength (Fig. S8). Remarkably, all
 140 these figures show that this process occurs for low wind velocities, typically
 141 for $u_* < 0.1 \text{ m s}^{-1}$. For shear velocities larger than 0.25 m s^{-1} , this wind
 142 reorientation does not occur. Finally, for intermediate shear velocities, both
 143 reorientation along the dune crest and no reorientation are observed (Fig. S7).

144 3 Influence of the circadian cycle of the atmospheric boundary 145 layer

146 For linear ridges, dune-induced flow disturbances have mainly been related
 147 to the angle between wind direction and crest orientation, with a maximum
 148 for angles between 30° and 70° (Walker et al. 2009; Hesp et al. 2015). In our
 149 case, the most deflected wind for both stations is the most perpendicular, such
 150 that the incident wind direction does not seem to be the dominant parameter
 151 controlling the wind deflection. In contrast, a different behavior is observed
 152 between low and high wind velocities, suggesting a change in hydrodynamical
 153 regime.

154 In the following, we discuss the relevant parameters leading to different
 155 hydrodynamical interactions with topographical obstacles, and interpret the
 156 data with respect to the corresponding physical mechanisms.

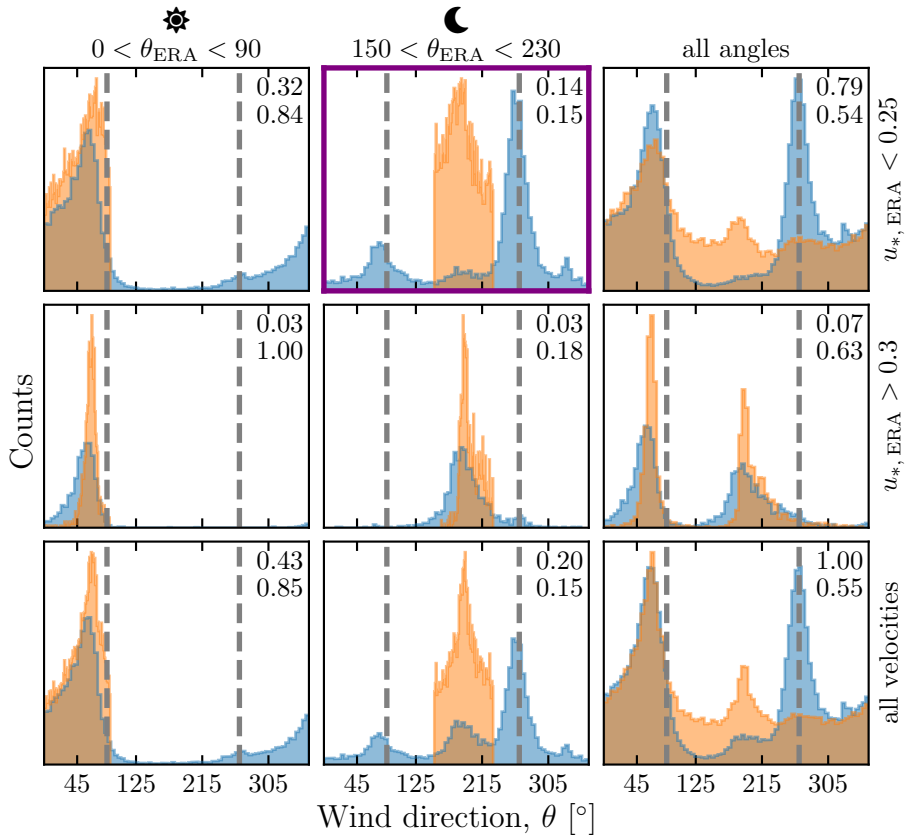


Fig. 3 Distributions of wind direction at the Deep Sea Station for the Era5Land climate reanalysis (orange) and the local measurements (blue). In each subplot, both distributions are plotted from the same time steps, selected with constraints on the wind direction (columns) and/or wind velocity (rows) of the Era5Land dataset. The gray vertical dashed lines indicate the dune orientation. The numbers at the top right give the percentage of time steps selected in each sub-range, as well as the percentage of them corresponding to the day (between 1000 UTC and 2200 UTC). The purple frame highlights the regime (small wind velocities, nocturnal summer wind) in which the data from both datasets differs. A similar figure can be obtained for the Deep Sea station (see Fig. S6).

157 3.1 Relevant non-dimensional parameters and physical considerations

158 Flow deflection over ridges can be understood from the Bernoulli principle (Hesp
 159 et al. 2015). As the flow approaches the ridge crest, the compression of the
 160 streamlines results in larger flow velocities, and thus lower pressures (Rubin
 161 and Hunter 1987). An incident flow oblique to the ridge is then deflected to-
 162 wards lower pressure zones, i.e towards the crest. Turbulent dissipation at the
 163 bottom and non-linearities tends to increase this effect downstream, resulting
 164 in along the crest wind deflection in the lee side (Hesp et al. 2015; Gadal et al.
 165 2019).

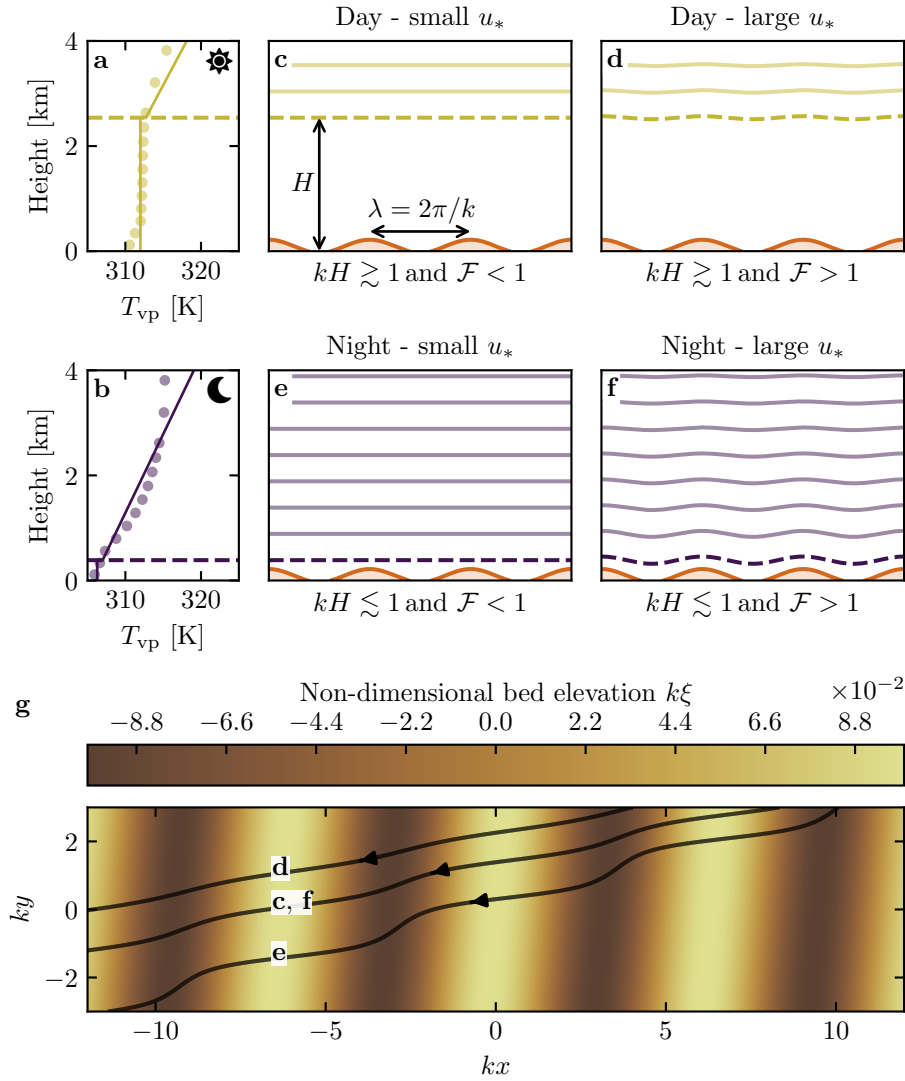


Fig. 4 **a–b:** Vertical profiles of the virtual potential temperature at 2 different time steps (day - 31/03/2017 - 1200 UTC, night - 21/03/2017 - 2200 UTC) at the Deep Sea station. Dots: data from the ERA5 reanalysis. Transparent dashed lines: boundary layer height given by the ERA5 reanalysis, calculated from the bulk Richardson number (Seidel et al. 2012). Plain lines: vertical (boundary layer) and linear (free atmosphere) fits to estimate the stratification properties. **c–f:** Sketches representing the interaction between the giant dunes and the atmospheric flow for different meteorological conditions. **g:** Streamlines qualitatively representing the effect of low, medium and high flow confinement. For details on the streamline derivation, see Appendix 4.

Another way to increase the flow deflection is its confinement below a capping surface, that results in further streamline compression. This is the case for bedforms forming in open channel flows such as rivers (Fourrière et al. 2010; Unsworth et al. 2018), but also for eolian dunes. These dunes evolve in the turbulent atmospheric boundary layer (ABL), which is capped by a transitional layer separating it from the stratified atmosphere above (see Fig. 4). Two different mechanisms control the possibility of this additional streamline compression.

On one hand, it depends if the flow disturbance induced by the underlying topography reach the surface. As obstacles typically disturb flow over a characteristic height similar to their length, the potential of interaction between the dunes and the overlying surface is well captured by the parameter kH , where $k = 2\pi/\lambda$ is the wavenumber and H the ABL depth. Note that H is directly related to the radiative fluxes at the Earth surface, and thus varies with the circadian and seasonal cycles. Here, the giant dunes have kilometric wavelengths, such that $0.02 \lesssim kH \lesssim 5$, and they interact most of the time with the capping layer and the stratified free atmosphere (FA) above (Andreotti et al. 2009). Interestingly, the limit of no-interactions between the topography and the boundary layer structure ($kH \gg 1$), in which the properties of the overlying atmospheric structure are irrelevant, is never reached here, in the case of giant dunes.

On the other hand, it depends on rigidity of the capping surface, as its deformation releases the confinement effect inducing streamline compression. This is typically quantified using the Froude number (Vosper 2004; Stull 2006; Sheridan and Vosper 2006; Hunt et al. 2006; Jiang 2014):

$$\mathcal{F} = \frac{U}{\sqrt{\frac{\Delta\rho}{\rho} g H}}, \quad (1)$$

where U is the wind velocity at the top of the ABL, ρ its average density, $\Delta\rho$ the density jump between the ABL and the FA.

The smallest wind disturbances are expected during the day, when the ABL depth is comparable to the dune wavelength ($kH \gtrsim 1$) and for large wind velocities, which correspond to a weak confinement situation (Fig. 4d). On the contrary, large wind disturbances are expected to occur during the night, when the confinement is mainly induced by shallow ABL (Fig. 4e–f). Note that this strong confinement can be somewhat reduced in the case of strong winds (corresponding to large Froude numbers, see Fig. 4f), explaining the transition from deflected to non-deflected winds related to low and high velocities observed in the data (see section 2.3).

3.2 Flow regime diagrams

To highlight these different regimes from our data, we compute wind disturbance diagrams in the space defined by the two relevant non-dimensional

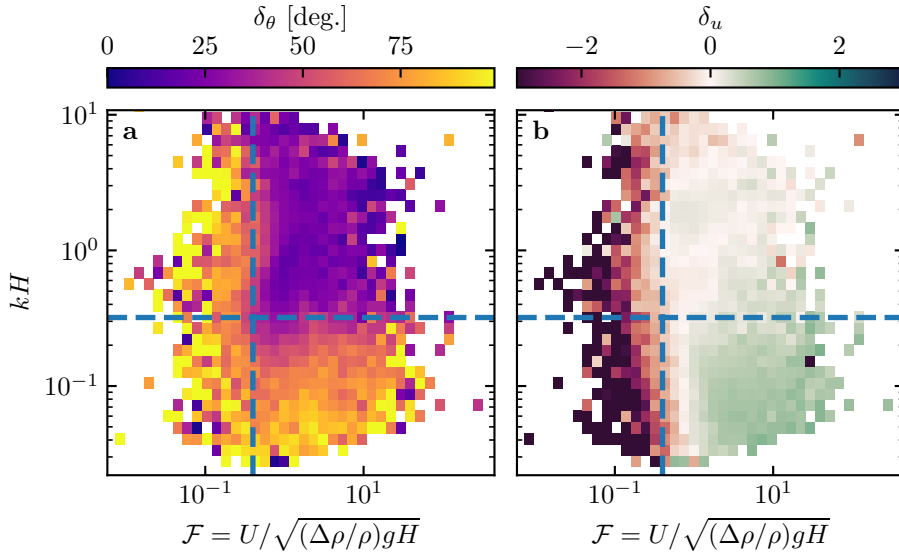


Fig. 5 Regime diagrams of the wind deviation δ_θ and relative attenuation/amplification δ_u in the space (\mathcal{F}, kH) , containing the data from both the Deep Sea and South Namib stations. Blue dashed lines empirically delimit the different regimes. The point density in each bin of the diagrams is shown in Fig. S11. The regime diagrams in the spaces (\mathcal{F}_1, kH) and $(\mathcal{F}_1, \mathcal{F})$ are shown in Fig. S12.

numbers presented above, (kH, \mathcal{F}) . Those are calculated from the time series of the geopotential, temperature and specific humidity vertical profiles available in the ERA5 climate reanalysis (see SI section 2). Flow deviation is computed as the minimal angle between the wind orientations from the local measurements, and the regional predictions. The relative velocity modulation is computed as

$$\delta_u = \frac{u_*^{\text{ERA}} - u_*^{\text{station}}}{u_*^{\text{ERA}}}. \quad (2)$$

When representing the two variables δ_θ and δ_u in this space, different regime emerges (Fig. 5). Small wind disturbances ($\delta_\theta \rightarrow 0, \delta_u \rightarrow 0$) are located in the top-right part of the diagrams, corresponding to a regime mixing low-interaction and low-confinement (kH and \mathcal{F} large enough, Fig. 4d). Lower values of kH (stronger interaction) or Froude number (stronger confinement) then both lead to an increase in wind disturbances, both in terms of orientation and velocity. Below a threshold value of $kH \simeq 0.3$, wind disturbance occurs independently of the Froude number value, probably due to enhanced non-linear effects linked to strong flow modulation by the obstacle in this part of the diagram. The Froude number also controls a transition from damped to amplified wind velocities in the interdune, with a transition at $\mathcal{F} \simeq 0.4$ (Fig. 5b). This may be linked to a transition in the flow regime in the lee side of the obstacle (lee waves, hydraulic jumps, rotors) but further measurements are needed in order to assess this (Baines 1995; Vosper 2004).

 225 3.3 On the influence of the stratification of the free atmosphere

226 The presence of a stratification in the free atmosphere can also impact the
 227 flow confinement, depending on its ability to deform under the presence of an
 228 underlying obstacle. This can be quantified using the internal Froude num-
 229 ber (Vosper 2004; Stull 2006; Sheridan and Vosper 2006; Hunt et al. 2006;
 230 Jiang 2014):

$$\mathcal{F}_I = \frac{kU}{N}, \quad (3)$$

231 where $N = \sqrt{-(g/\rho)(\partial\rho/\partial z)}$ is characteristic of the stratification. Both Froude
 232 numbers have the same qualitative effect on flow confinement, as they quan-
 233 tify the rigidity of the overlying layers. This is confirmed by figure S12, where
 234 we can also find the different regimes related to wind disturbances described
 235 previously for the Froude number \mathcal{F} .

236 **4 Discussion**

237 The comparison of local (direct measurements) and regional (climate reanal-
 238 ysis) wind data reveals the giant dunes feedback on the flow. In flat areas,
 239 the matching between measurements and prediction confirms the ability of the
 240 ERA5Land climate reanalysis to predict the wind flow down to scales ~ 10 km,
 241 i.e the grid model. When smaller scale topographies are present (giant dunes
 242 in our case), locally measured wind regimes can significantly differ from the
 243 regionally predicted ones. Furthermore, we link these disturbances induced by
 244 the dunes to their interaction with the lower part of the atmospheric vertical
 245 structure, and more specifically to its circadian variability. During the night,
 246 the presence of a shallow atmospheric boundary layer (ABL) induces a strong
 247 confinement of the flow, associated with large wind deviation and acceleration
 248 or deceleration. During the day, the capping layer is high enough to prevent
 249 its interaction with the giant dunes, resulting in a low confinement of the flow,
 250 and thus smaller wind disturbances. Interestingly, we also found that this ef-
 251 fect could be counterbalanced by the presence of large wind velocities, capable
 252 of deforming the capping layer and/or the FA stratification, thus decreasing
 253 the confinement effect.

254 Simple linear models also suggest that larger wind disturbances occur un-
 255 der strong flow confinement such as described above Andreotti et al. (2009,
 256 2012). However, they are unable to reproduce the magnitude of the observed
 257 deviations, probably due to the presence of hydrodynamical non-linear effects,
 258 all the more present in high confinement situations linked to strong flow mod-
 259 ulations (see Fig. S12 and Appendix 1). They also predict different spatial flow
 260 structures such as lee waves and rotors (Baines 1995; Vosper 2004), which are
 261 likely to be complicated by these non-linearities, and which cannot be observed
 262 by our single point measurements. Measurements in different places along and
 263 across the ridge are then needed in order to properly map these flow structures,
 264 and allow further comparisons with models.

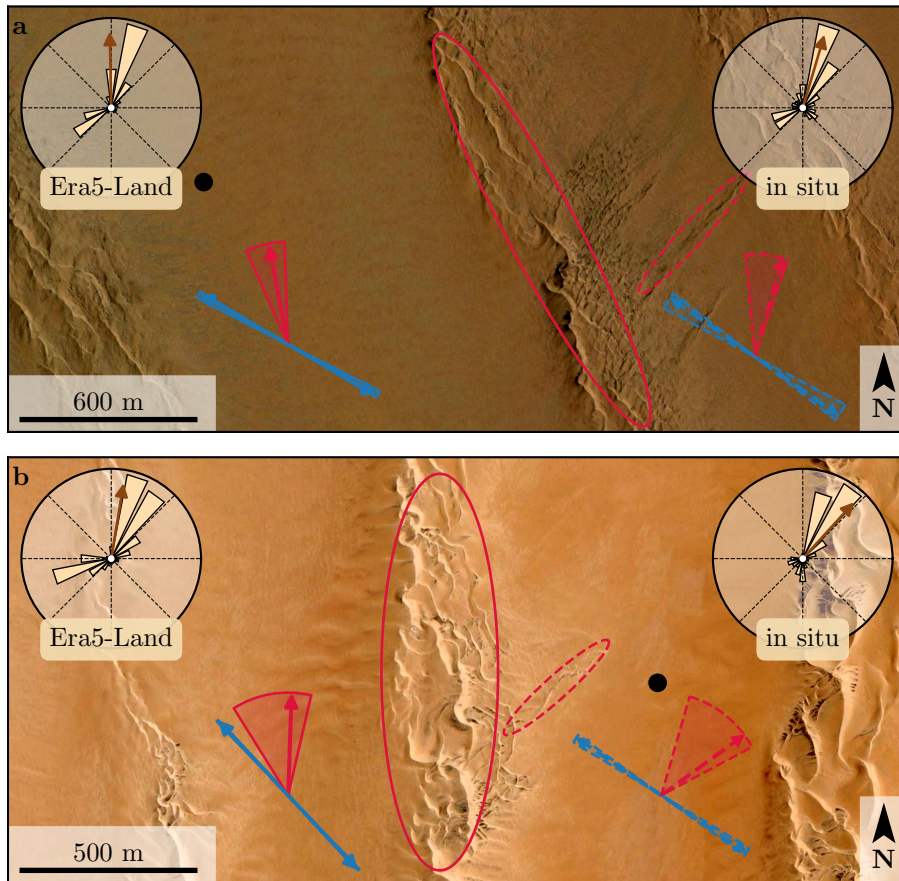


Fig. 6 Implications for smaller scale patterns in (a) the South Namib and (b) Deep Sea. The ellipses indicates the different types of elongating dunes, at large (plain) and small scale (dashed). The dune orientations are calculated using the model of Courrech du Pont et al. (2014) from the sand flux angular distributions, shown here for typical sand quartz grains of $180\ \mu\text{m}$. The double blue and single red arrows correspond to the two possible dune growth mechanisms, bed instability and elongation, respectively. Likewise, plain arrows are calculated from the ERA5-Land data, and dashed arrows from the local measurements. Wedges show the uncertainty on the orientation calculation, and the arrows correspond to typical parameters found in the literature, i.e. a grain diameter of $180\ \mu\text{m}$ and a flux-up ratio of 1.6. The black dots indicate the position of the measurement stations. See Appendix 2 for additional details.

This study highlights the interaction between giant dunes and the atmospheric boundary layer. It then supports the debated idea that the capping layer acts as a bounding surface limiting dune growth (Andreotti et al. 2009), as opposed to an unconstrained growth ever-slower with size (Eastwood et al. 2011; Gunn et al. 2021). Once validated, this mechanism would then allow inference of the ABL depth from the giant bedforms spacing where measure-

271 ments are not feasible or available, as performed by Lorenz et al. (2010) on
 272 Titan.

273 This interaction also have strong implications for smaller scales bedforms,
 274 as illustrated in Fig. 6. In the Namib Sand Sea, small linear dunes (~ 50 m
 275 -wide) are present in the interdune between giant linear dunes (~ 2 km -wide).
 276 While differences between larger and smaller scale dune patterns are observed
 277 ubiquitously, they are now largely attributed to the presence of two different
 278 dune growth mechanisms, leading to two different dune patterns (orientations
 279 and/or morphologies) for the same wind regime (Courrech du Pont et al.
 280 2014; Runyon et al. 2017; Lü et al. 2017; Song et al. 2019; Hu et al. 2021).
 281 Here, coupling sediment transport and dune growth models, we show that the
 282 orientations of the small and giant linear dunes can be predicted from the same
 283 dune growth mechanism, using the locally measured and regionally predicted
 284 winds, respectively (red arrows in Fig. 6). The giant dune feedback on the
 285 flow described in this study then provides a mechanism for the existence of
 286 these small linear dunes elongating across the interdune, as yet unresolved.
 287 While further studies are needed, these dune type could provide additional
 288 strong constraints for the inference of local winds from bedforms, as currently
 289 performed on Mars using ripple orientations (Liu and Zimbelman 2015; Hood
 290 et al. 2021).

291 **Acknowledgements** [citing all grants ...]

292 Finally, we would like to acknowledge the contributors of the following open-source python
 293 librairies, Matplotlib (Hunter 2007), Numpy (Harris et al. 2020) and Scipy (Virtanen et al.
 294 2020), which provide an incredibly efficient ecosystem allowing scientific research in Python.

295 **Appendix 1: ABL turbulent wind model**

296 Following the work of Fourrière et al. (2010), Andreotti et al. (2012) and Andreotti et al. (2009), we briefly expose in this section the linear response of a
 297 turbulent flow to a small aspect ratio perturbation of the underlying topogra-
 298 phy. As this topography can be decomposed into several sinusoidal modes, we
 299 focus on a sinusoidal topography:

$$\xi = \xi_0 \cos [k (\cos(\alpha)x + \sin(\alpha)y)], \quad (4)$$

300 which is also a good approximation for the giant dunes observed in the Deep
 301 Sea and South Namib Station (see Fig 1 and Fig S4). Here, x and y are
 302 the streamwise and spanwise coordinates, $k = 2\pi/\lambda$ the wavenumber of the
 303 sinusoidal perturbation, and α its crest orientation, calculated with respect to
 304 the y -direction.

305 The two components of the basal shear stress $\tau = \rho u_* \mathbf{u}_*$, constant in a
 306 flat bottom situation, can then be written without loss of generality as:

$$\tau_x = \tau_0 \left(1 + k \xi_0 \sqrt{\mathcal{A}_x^2 + \mathcal{B}_x^2} \cos [k (\cos(\alpha)x + \sin(\alpha)y) + \phi_x] \right), \quad (5)$$

$$\tau_y = \tau_0 k \xi_0 \sqrt{\mathcal{A}_y^2 + \mathcal{B}_y^2} \cos [k (\cos(\alpha)x + \sin(\alpha)y) + \phi_y], \quad (6)$$

308 where τ_0 is the basal shear stress on a flat bed, and $\phi_{x,y} = \tan^{-1}(\mathcal{B}_{x,y}/\mathcal{A}_{x,y})$.
 309 The in-phase and in-quadrature hydrodynamical coefficients $\mathcal{A}_{x,y}$ and $\mathcal{B}_{x,y}$
 310 are functions of the flow conditions, i.e the bottom roughness, the vertical
 311 flow structure or the incident flow direction (Fourrière et al. 2010; Andreotti
 312 et al. 2009, 2012).

313 Following Andreotti et al. (2012), the impact of the incident wind direction
 314 can be approximated by the following expressions:

$$\mathcal{A}_x = \mathcal{A}_0 \cos^2 \alpha, \quad (7)$$

$$\mathcal{B}_x = \mathcal{B}_0 \cos^2 \alpha, \quad (8)$$

$$\mathcal{A}_y = \frac{1}{2} \mathcal{A}_0 \cos \alpha \sin \alpha, \quad (9)$$

$$\mathcal{B}_y = \frac{1}{2} \mathcal{B}_0 \cos \alpha \sin \alpha, \quad (10)$$

315 where \mathcal{A}_0 and \mathcal{B}_0 are now two coefficients independent of the dune orientation
 316 α . In the case of a fully turbulent boundary layer capped by a stratified atmo-
 317 sphere, they now only depend on kH , kz_0 , \mathcal{F} and \mathcal{F}_I Andreotti et al. (2009).
 318 In this study, we assume a constant hydrodynamic roughness $z_0 \sim 1$ mm,
 319 leading to a constant value of $kz_0 \sim 10^{-6}$. Measured values of z_0 in the field
 320 indeed reports a variation of z_0 between 0.1 mm and 10 mm (Sherman and
 321 Farrell 2008; Field and Pelletier 2018), but \mathcal{A}_0 and \mathcal{B}_0 does not vary much in
 322 the corresponding range of kz_0 (Fourrière et al. 2010). Note that the linearity
 323 assumption of this theoretical framework requires $(|\tau| - \tau_0)/\tau_0 \ll 1$, which is
 324 satisfied by $k\xi \sqrt{\mathcal{A}_0^2 + \mathcal{B}_0^2} \ll 1$. In our case, the giant dune morphology gives
 325 $k\xi \simeq 0.1$, setting the upper bound of the coefficient modulus $\sqrt{\mathcal{A}_0^2 + \mathcal{B}_0^2}$ to 10.

326 Additionally, we also calculate the time series of the hydrodynamical coeffi-
 327 cients from the time series of the non-dimensional numbers used in this study.
 328 The results, shown Fig. S12 under the similar form of the regime diagrams
 329 presented in Fig. 5 and Fig. S12, exhibit a qualitative matching with the ob-
 330 servations presented in this study. Small values of these coefficients ($\mathcal{A}_0 \simeq 3.4$
 331 and $\mathcal{B}_0 \simeq 1$) are found in low confinement cases, i.e for $kH \gg 1$ (no inter-
 332 action between the dunes and the capping layer) or for $kH \gg 1$ but large
 333 enough Froude numbers (reduced flow confinement due to the deformation of
 334 the overlying capping layer and stratification). In contrast, larger values are
 335 obtained in high confinement cases (small kH and Froude numbers). How-
 336 ever, not that most of this part of the diagrams are outside of the linear limit
 337 discussed above ($\sqrt{\mathcal{A}_0^2 + \mathcal{B}_0^2} \gtrsim 10$), which does not allow further quantitative
 338 comparison with the data.

339 Appendix 2: Sediment transport and dune morphodynamics

340 Here, we briefly describe the sediment transport and dune morphodynamics
 341 theoretical framework leading to the prediction of sand fluxes and dune ori-
 342 entations from wind data.

Sediment transport The prediction of sand fluxes from wind data has been a long standing issue in geomorphological studies (Fryberger and Dean 1979; Pearce and Walker 2005; Sherman and Li 2012; Shen et al. 2019). Based on laboratory studies in wind tunnels (Rasmussen et al. 1996; Iversen and Rasmussen 1999; Creyssels et al. 2009; Ho et al. 2011), as well as physical considerations (Ungar and Haff 1987; Andreotti 2004; Durán et al. 2011; Pähzt and Durán 2020), it has been shown that the steady saturated sand flux over a flat sand bed depends linearly on the shear stress:

$$\frac{q_{\text{sat}, t}}{Q} = \Omega \sqrt{\Theta_{\text{th}}} (\Theta_t - \Theta_{\text{th}}), \quad (11)$$

where Ω is a proportionality constant, $Q = d\sqrt{(\rho_s - \rho)gd/\rho}$ is a characteristic flux, $\Theta = \rho u_{*,t}^2 / ((\rho_s - \rho)gd)$ the Shields number, and Θ_{th} its threshold value for incipient sediment transport. Here, $\rho_s = 2.6 \text{ g cm}^{-3}$ and $d = 180 \mu\text{m}$ are the grain density and diameter, and g is the gravitational acceleration.

Recently, Pähzt and Durán (2020) suggested a quadratic dependency on the shear stress by taking into account grain–grain interactions within the transport layer, performing better at reproducing laboratory data at high wind velocities:

$$\frac{q_{\text{sat}, t}}{Q} = \frac{2\sqrt{\Theta_{\text{th}}}}{\kappa\mu} (\Theta_t - \Theta_{\text{th}}) \left(1 + \frac{C_M}{\mu} [\Theta_t - \Theta_{\text{th}}] \right), \quad (12)$$

where $\kappa = 0.4$ is the von Kármán constant, $C_M = 1.7$ a constant and μ a friction coefficient, taken to be the avalanche slope of the granular material, i.e. ~ 0.6 . The fit of this law to the experimental data of Creyssels et al. (2009) and Ho et al. (2011) gives $\Theta_{\text{th}} = 0.0035$. The sand flux angular distributions and the dune orientations in Fig. 6 are calculated using this quartic law (12). However, we verified that using the quadratic law (11) instead did not change the predicted dune orientations by more than a few degrees.

Dune orientations The dune orientations are predicted from the computed sand flux time series, using the dimensional model of Courrech du Pont et al. (2014). Two orientations are possible depending on the mechanism dominating the dune growth: elongation or bed instability (the latter is also known as the rule of maximum gross bedform-normal transport from Rubin and Hunter (1987)).

The orientation α corresponding the bed instability is then the one that maximizes the following growth rate:

$$\sigma \propto \frac{1}{H_d W_d T} \int_t q_{\text{crest},t} |\sin(\theta_t - \alpha)|, \quad (13)$$

where H_d and W_d are dimensional constants representing the dune height and width, respectively. The flux at the crest is expressed as:

$$q_{\text{crest},t} = q_{\text{sat},t} [1 + \gamma |\sin(\theta_t - \alpha)|], \quad (14)$$

376 where the flux-up ratio γ has been calibrated to 1.6 using field studies, under-
 377 water laboratory experiments and numerical simulations. Similarly, the dune
 378 orientation corresponding to the elongation mechanism is the one that verifies:

$$\tan(\alpha) = \frac{\langle q_{\text{crest},t}(\alpha) \mathbf{e}_{\theta_t} \rangle \cdot \mathbf{e}_{WE}}{\langle q_{\text{crest},t}(\alpha) \mathbf{e}_{\theta_t} \rangle \cdot \mathbf{e}_{SN}}, \quad (15)$$

379 where $\langle . \rangle$ denotes a vectorial time average. The unitary vectors \mathbf{e}_{WE} , \mathbf{e}_{SN} and
 380 \mathbf{e}_{θ_t} are in the West–East, South–North and wind direction, respectively.

381 The resulting computed dune orientations, blue and red arrows in figure 6,
 382 are then depending on a certain number of parameters (grain properties, flux-
 383 up ratio), for which we took typical values for eolian desert on Earth. Due to
 384 the lack of measurements in the studied places, significant uncertainties can
 385 however be expected. We therefore run a sensibility test by calculating the
 386 dune orientations for grain diameters ranging from 100 μm to 400 μm and the
 387 speed-up ratio from 0.1 to 10 (wedges on figure 6).

388 References

- 389 Andreotti B (2004) A two-species model of aeolian sand transport. *J Fluid
390 Mech* 510(510):47–70, DOI 10.1017/S0022112004009073
- 391 Andreotti B, Fourrière A, Ould-Kaddour F, Murray B, Claudin P (2009) Gi-
392 ant aeolian dune size determined by the average depth of the atmospheric
393 boundary layer. *Nature* 457(7233):1120–1123
- 394 Andreotti B, Claudin P, Devauchelle O, Durán O, Fourrière A (2012) Bedforms
395 in a turbulent stream: ripples, chevrons and antidunes. *Journal of Fluid
396 Mechanics* 690:94–128
- 397 Ashkenazy Y, Yizhaq H, Tsoar H (2012) Sand dune mobility under climate
398 change in the kalahari and australian deserts. *Climatic Change* 112(3):901–
399 923
- 400 Bacik KA, Lovett S, Colm-cille PC, Vriend NM (2020) Wake induced long
401 range repulsion of aqueous dunes. *Physical review letters* 124(5):054,501
- 402 Baines PG (1995) Topographic effects in stratified flows. Cambridge university
403 press
- 404 Blumberg DG, Greeley R (1996) A comparison of general circulation model
405 predictions to sand drift and dune orientations. *Journal of Climate*
406 9(12):3248–3259
- 407 Claudin P, Wiggs GFS, Andreotti B (2013) Field evidence for the upwind
408 velocity shift at the crest of low dunes. *Boundary-layer Meteorol* 148(1):195–
409 206, DOI 10.1007/s10546-013-9804-3
- 410 Courrech du Pont S (2015) Dune morphodynamics. *Comptes Rendus Physique*
411 16(1):118–138
- 412 Courrech du Pont S, Narteau C, Gao X (2014) Two modes for dune orientation.
413 *Geology* 42(9):743–746
- 414 Creyssels M, Dupont P, El Mohtar AO, Valance A, Cantat I, Jenkins JT, Pasini
415 JM, Rasmussen KR (2009) Saltating particles in a turbulent boundary layer:
416 experiment and theory. *Journal of Fluid Mechanics* 625:47–74
- 417 Dee DP, Uppala SM, Simmons AJ, Berrisford P, Poli P, Kobayashi S, Andrae
418 U, Balmaseda M, Balsamo G, Bauer dP, et al. (2011) The era-interim re-
419 analysis: Configuration and performance of the data assimilation system.
420 *Quarterly Journal of the royal meteorological society* 137(656):553–597
- 421 Durán O, Claudin P, Andreotti B (2011) On aeolian transport: Grain-scale
422 interactions, dynamical mechanisms and scaling laws. *Aeolian Research*
423 3(3):243–270, DOI 10.1016/j.aeolia.2011.07.006
- 424 Durran DR (1990) Mountain waves and downslope winds. In: *Atmospheric
425 processes over complex terrain*, Springer, pp 59–81
- 426 Eastwood E, Nield J, Baas A, Kocurek G (2011) Modelling controls on aeolian
427 dune-field pattern evolution. *Sedimentology* 58(6):1391–1406
- 428 Farr TG, Rosen PA, Caro E, Crippen R, Duren R, Hensley S, Kobrick M,
429 Paller M, Rodriguez E, Roth L, et al. (2007) The shuttle radar topography
430 mission. *Reviews of geophysics* 45(2)
- 431 Fernando H, Mann J, Palma J, Lundquist JK, Barthelmie RJ, Belo-Pereira M,
432 Brown W, Chow F, Gerz T, Hocut C, et al. (2019) The perdigao: Peering

- 433 into microscale details of mountain winds. *Bulletin of the American Meteorological Society* 100(5):799–819
434
- 435 Field JP, Pelletier JD (2018) Controls on the aerodynamic roughness length
436 and the grain-size dependence of aeolian sediment transport. *Earth Surface
437 Processes and Landforms* 43(12):2616–2626, DOI 10.1002/esp.4420
- 438 Fourrière A, Claudin P, Andreotti B (2010) Bedforms in a turbulent stream:
439 formation of ripples by primary linear instability and of dunes by nonlinear
440 pattern coarsening. *Journal of Fluid Mechanics* 649:287–328
- 441 Frederick KA, Hanratty TJ (1988) Velocity measurements for a turbulent non-
442 separated flow over solid waves. *Experiments in fluids* 6(7):477–486
- 443 Fryberger SG, Dean G (1979) Dune forms and wind regime. A study of global
444 sand seas 1052:137–169
- 445 Gadal C, Narteau C, Courrech Du Pont S, Rozier O, Claudin P (2019) Incip-
446 ient bedforms in a bidirectional wind regime. *Journal of Fluid Mechanics*
447 862:490–516
- 448 Gunn A, Wanker M, Lancaster N, Edmonds DA, Ewing RC, Jerolmack DJ
449 (2021) Circadian rhythm of dune-field activity. *Geophysical Research Letters*
450 48(5):e2020GL090,924
- 451 Harris CR, Millman KJ, van der Walt SJ, Gommers R, Virtanen P, Cournapeau D,
452 Wieser E, Taylor J, Berg S, Smith NJ, et al. (2020) Array program-
453 ming with numpy. *Nature* 585(7825):357–362
- 454 Hersbach H, Bell B, Berrisford P, Hirahara S, Horányi A, Muñoz-Sabater
455 J, Nicolas J, Peubey C, Radu R, Schepers D, et al. (2020) The era5
456 global reanalysis. *Quarterly Journal of the Royal Meteorological Society*
457 146(730):1999–2049
- 458 Hesp PA, Smyth TAG, Nielsen P, Walker IJ, Bauer BO, Davidson-Arnott R
459 (2015) Flow deflection over a foredune. *Geomorphology* 230:64–74
- 460 Ho TD, Valance A, Dupont P, Ould El Moctar A, Tuan Duc H, Valance A,
461 Dupont P, Ould El Moctar A (2011) Scaling laws in aeolian sand transport.
462 *Physical Review Letters* 106(9):4–7, DOI 10.1103/PhysRevLett.106.094501
- 463 Hood DR, Ewing RC, Roback KP, Runyon K, Avouac JP, McEnroe M (2021)
464 Inferring airflow across martian dunes from ripple patterns and dynamics.
465 *Frontiers in Earth Science* 9:Art-No
- 466 Howard AD (1977) Effect of slope on the threshold of motion and its applica-
467 tion to orientation of wind ripples. *Geological Society of America Bulletin*
468 88(6):853–856
- 469 Hu Z, Gao X, Lei J, Zhou N (2021) Geomorphology of aeolian dunes in the
470 western sahara desert. *Geomorphology* 392:107,916
- 471 Hunt J, Leibovich S, Richards K (1988) Turbulent shear flows over low hills.
472 *Quarterly Journal of the Royal Meteorological Society* 114(484):1435–1470
- 473 Hunt JCR, Vilenski GG, Johnson ER (2006) Stratified separated flow around
474 a mountain with an inversion layer below the mountain top. *Journal of Fluid
475 Mechanics* 556:105–119
- 476 Hunter JD (2007) Matplotlib: A 2d graphics environment. *Computing in sci-
477 ence & engineering* 9(03):90–95

- 478 Iversen JD, Rasmussen KR (1999) The effect of wind speed and bed slope on
479 sand transport. *Sedimentology* 46:723–731
- 480 Jackson PS, Hunt JCR (1975) Turbulent wind flow over a low hill. *Quarterly
481 Journal of the Royal Meteorological Society* 101(430):929–955
- 482 Jiang Q (2014) Applicability of reduced-gravity shallow-water theory to
483 atmospheric flow over topography. *Journal of the Atmospheric Sciences*
484 71(4):1460–1479
- 485 Jolivet M, Braucher R, Dovchintseren D, Hocquet S, Schmitt J, ASTER Team
486 (2021) Erosion around a large-scale topographic high in a semi-arid sedimen-
487 tary basin: Interactions between fluvial erosion, aeolian erosion and aeolian
488 transport. *Geomorphology* 386:107,747
- 489 Kim HG, Patel VC, Lee CM (2000) Numerical simulation of wind flow
490 over hilly terrain. *Journal of wind engineering and industrial aerodynamics*
491 87(1):45–60
- 492 Lancaster LNSM J (1984) Climate of the central namib desert. *Madoqua*
493 1984(1):5–61
- 494 Lancaster N (1985) Winds and sand movements in the namib sand sea. *Earth
495 Surface Processes and Landforms* 10(6):607–619
- 496 Lewis HW, Mobbs SD, Lehning M (2008) Observations of cross-ridge flows
497 across steep terrain. *Quarterly Journal of the Royal Meteorological Society:
498 A journal of the atmospheric sciences, applied meteorology and physical
499 oceanography* 134(633):801–816
- 500 Liu ZYC, Zimbelman JR (2015) Recent near-surface wind directions inferred
501 from mapping sand ripples on martian dunes. *Icarus* 261:169–181
- 502 Livingstone I, Warren A (1996) Aeolian geomorphology: an introduction. Ad-
503 dison Wesley Longman Ltd
- 504 Livingstone I, Bristow C, Bryant RG, Bullard J, White K, Wiggs GFS, Baas
505 ACW, Bateman MD, Thomas DSG (2010) The namib sand sea digital
506 database of aeolian dunes and key forcing variables. *Aeolian Research* 2(2-
507 3):93–104
- 508 Lorenz R, Claudin P, Andreotti B, Radebaugh J, Tokano T (2010) A 3 km
509 atmospheric boundary layer on titan indicated by dune spacing and huygens
510 data. *Icarus* 205(2):719–721
- 511 Lü P, Narteau C, Dong Z, Rozier O, Du Pont SC (2017) Unravelling raked
512 linear dunes to explain the coexistence of bedforms in complex dunefields.
513 *Nature communications* 8(1):1–9
- 514 Lü P, Narteau C, Dong Z, Claudin P, Rodriguez S, An Z, Fernandez-Cascales
515 L, Gadale C, Courrech du Pont S (2021) Direct validation of dune instability
516 theory. *Proceedings of the National Academy of Sciences* 118(17)
- 517 McKee ED (1979) A study of global sand seas, vol 1052. US Government
518 Printing Office
- 519 Muñoz-Sabater J, Dutra E, Agustí-Panareda A, Albergel C, Arduini G, Bal-
520 samo G, Boussetta S, Choulga M, Harrigan S, Hersbach H, et al. (2021)
521 Era5-land: A state-of-the-art global reanalysis dataset for land applications.
522 *Earth System Science Data Discussions* pp 1–50

- 523 Pähzt T, Durán O (2020) Unification of aeolian and fluvial sediment transport
524 rate from granular physics. *Physical review letters* 124(16):168,001
- 525 Pearce KI, Walker IJ (2005) Frequency and magnitude biases in the 'Fryberger'
526 model, with implications for characterizing geomorphically effective winds.
527 *Geomorphology* 68(1-2):39–55, DOI 10.1016/j.geomorph.2004.09.030
- 528 Rasmussen KR, Iversen JD, Rautaheimo P (1996) Saltation and wind flow
529 interaction in a variable slope wind tunnel. *Geomorphology* 17:19–28
- 530 Rubin DM, Hunter RE (1987) Bedform alignment in di-
531 rectinally varying flows. *Science* 237:276–278, DOI
532 <https://doi.org/10.1126/science.237.4812.276>
- 533 Runyon K, Bridges N, Ayoub F, Newman C, Quade J (2017) An integrated
534 model for dune morphology and sand fluxes on mars. *Earth and Planetary
535 Science Letters* 457:204–212
- 536 Seidel DJ, Zhang Y, Beljaars A, Golaz JC, Jacobson AR, Medeiros B (2012)
537 Climatology of the planetary boundary layer over the continental united
538 states and europe. *Journal of Geophysical Research: Atmospheres* 117(D17)
- 539 Shen Y, Zhang C, Huang X, Wang X, Cen S (2019) The effect of wind speed
540 averaging time on sand transport estimates. *Catena* 175:286–293
- 541 Sheridan PF, Vosper SB (2006) A flow regime diagram for forecasting lee
542 waves, rotors and downslope winds. *Meteorological Applications* 13(2):179–
543 195
- 544 Sherman DJ, Farrell EJ (2008) Aerodynamic roughness lengths over movable
545 beds: Comparison of wind tunnel and field data. *Journal of Geophysical
546 Research: Earth Surface* 113(2):1–10, DOI 10.1029/2007JF000784
- 547 Sherman DJ, Li B (2012) Predicting aeolian sand transport rates: A reevalu-
548 ation of models. *Aeolian Research* 3(4):371–378
- 549 Smith AB, Jackson DWT, Cooper JAG (2017) Three-dimensional airflow and
550 sediment transport patterns over barchan dunes. *Geomorphology* 278:28–42
- 551 Song Q, Gao X, Lei J, Li S (2019) Spatial distribution of sand dunes and their
552 relationship with fluvial systems on the southern margin of the taklimakan
553 desert, china. *Geomatics, Natural Hazards and Risk* 10(1):2408–2428
- 554 Stull R (2006) 9 - the atmospheric boundary layer. In: Wallace JM, Hobbs
555 PV (eds) *Atmospheric Science* (Second Edition), second edition edn, Aca-
556 demic Press, San Diego, pp 375–417, DOI <https://doi.org/10.1016/B978-0-12-732951-2.50014-4>
- 558 Stull RB (1988) An introduction to boundary layer meteorology, vol 13.
559 Springer Science & Business Media
- 560 Sullivan PP, McWilliams JC (2010) Dynamics of winds and currents coupled
561 to surface waves. *Annual Review of Fluid Mechanics* 42:19–42
- 562 Sykes RI (1980) An asymptotic theory of incompressible turbulent boundary-
563 layer flow over a small hump. *Journal of Fluid Mechanics* 101(3):647–670
- 564 Tritton D (2012) *Physical fluid dynamics*. Springer Science & Business Media
- 565 Ungar JE, Haff PK (1987) Steady state saltation in air. *Sedimentology* 34:289–
566 299
- 567 Unsworth C, Parsons D, Hardy R, Reesink A, Best J, Ashworth P, Keevil G
568 (2018) The impact of nonequilibrium flow on the structure of turbulence

- 569 over river dunes. *Water Resources Research* 54(9):6566–6584
570 Uppala SM, Källberg P, Simmons AJ, Andrae U, Bechtold VDC, Fiorino M,
571 Gibson J, Haseler J, Hernandez A, Kelly G, et al. (2005) The era-40 re-
572 analysis. *Quarterly Journal of the Royal Meteorological Society: A journal*
573 of the atmospheric sciences, applied meteorology and physical oceanography
574 131(612):2961–3012
575 Virtanen P, Gommers R, Oliphant TE, Haberland M, Reddy T, Cournapeau
576 D, Burovski E, Peterson P, Weckesser W, Bright J, et al. (2020) Scipy 1.0:
577 fundamental algorithms for scientific computing in python. *Nature methods*
578 17(3):261–272
579 Vosper SB (2004) Inversion effects on mountain lee waves. *Quarterly Journal*
580 of the Royal Meteorological Society: A journal of the atmospheric sciences,
581 applied meteorology and physical oceanography 130(600):1723–1748
582 Walker IJ, Shugar DH (2013) Secondary flow deflection in the lee of transverse
583 dunes with implications for dune morphodynamics and migration. *Earth*
584 *surface processes and landforms* 38(14):1642–1654
585 Walker IJ, Hesp PA, Davidson-Arnott RG, Bauer BO, Namikas SL,
586 Ollerhead J (2009) Responses of three-dimensional flow to variations
587 in the angle of incident wind and profile form of dunes: Greenwich
588 dunes, prince edward island, canada. *Geomorphology* 105:127–138, DOI
589 10.1016/j.geomorph.2007.12.019
590 Zilker DP, Hanratty TJ (1979) Influence of the amplitude of a solid wavy wall
591 on a turbulent flow. part 2. separated flows. *Journal of Fluid Mechanics*
592 90(2):257–271
593 Zilker DP, Cook GW, Hanratty TJ (1977) Influence of the amplitude of a solid
594 wavy wall on a turbulent flow. part 1. non-separated flows. *Journal of Fluid*
595 *Mechanics* 82(1):29–51

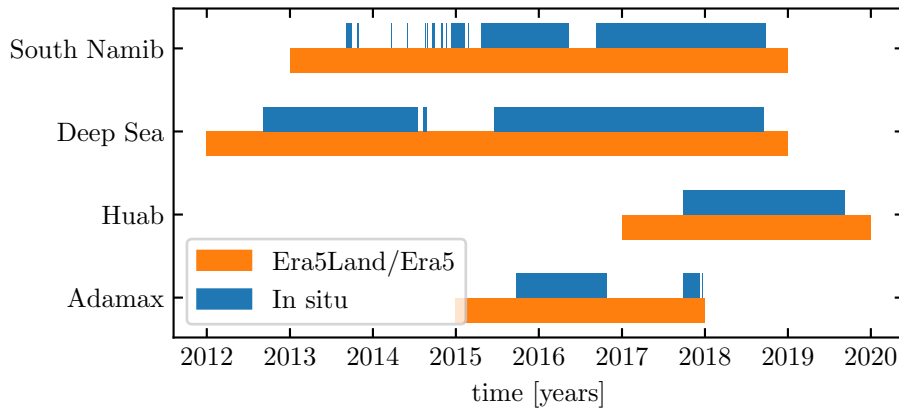


Fig. S1 Gant chart representing the valid time steps for the two data sets, for all stations.

596 **Supplementary Material for *Boundary-Layer Meteorology* Sample
597 Paper: Instructions for Authors**

598 **First Author* · Second Author · Third Author**

599
600 *Affiliation and email address for the corresponding author only (note that
601 the corresponding author does not need to be the first author).

602 **1. Shear velocity and calibration of the hydrodynamical roughness**

603 For each station, the hydrodynamic roughness is calibrated by finding the
604 one that minimizes the relative difference δ between the wind vectors of both
605 datasets:

$$\delta = \frac{\sqrt{\langle \| \mathbf{u}_{*,\text{era}} - \mathbf{u}_{*,\text{station}} \|^2 \rangle_t}}{\sqrt{\langle \| \mathbf{u}_{*,\text{era}} \|^2 \rangle_t \langle \| \mathbf{u}_{*,\text{station}} \|^2 \rangle_t}} \quad (16)$$

606 This δ -parameter is computed for hydrodynamic roughness values ranging
607 from 10^{-5} m to 10^{-2} m for the different stations. As shown by figure S3,
608 the minimum of δ in the space ($z_0, \text{Era}, z_0, \text{in situ}$) forms a line. We thus take
609 the roughness of the Era5Land dataset as the typical value when sediment
610 transport occurs, 10^{-3} m, corresponding to the thickness of the transport
611 layer (Durán et al. 2011). It leads for the Adamax, Deep Sea, Huab and South
612 Namib stations values of 2.7 mm, 0.76 mm, 0.12 mm and 0.48 mm, respectively.

613 The choice of the hydrodynamic roughness values only impacts the cal-
614 culated shear velocities, but note the wind directions. As such, most of our
615 conclusions are then independent of such a choice, and only the magnitude of
616 the wind velocity attenuation in confined situation might be affected.

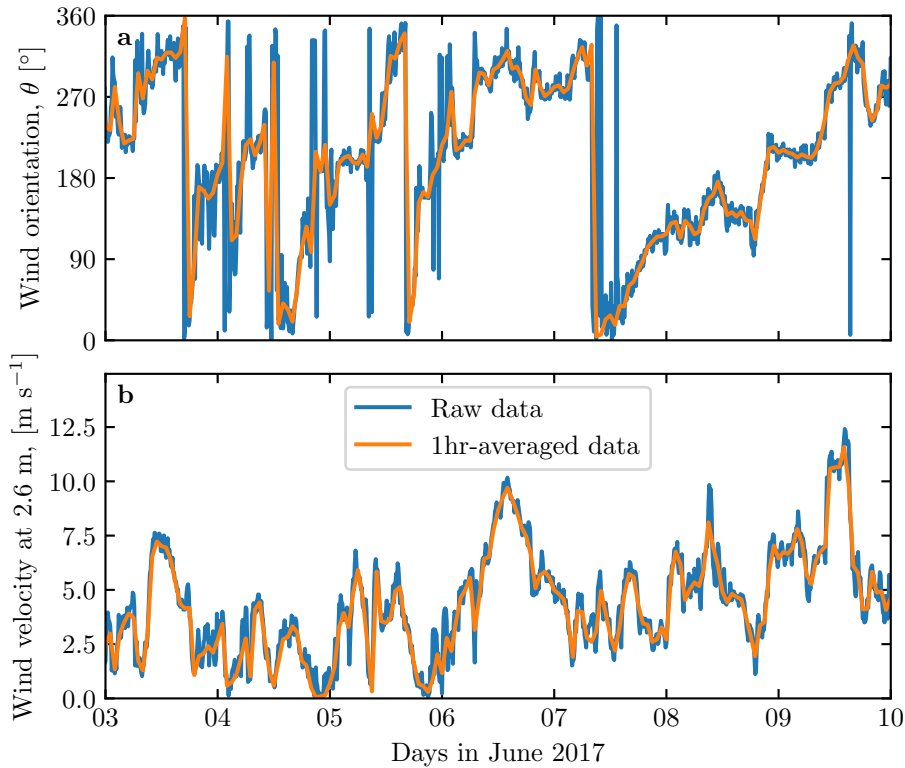


Fig. S2 Comparison between raw local wind measurements, and centered averaged data over one hour for the South Namib station. **a:** wind direction. **b:** wind velocity at the measurement height, 2.6 m.

617 2. Extraction of the ABL properties

618 In order to estimate the relevant non-dimensional numbers, one need to es-
 619 timate in addition to the wind and dune properties some parameters of the
 620 ABL. The Era5 dataset provides a direct bulk estimate of the ABL depth H
 621 from a bulk Richardson number calculation, as well as vertical profiles of the
 622 geopotential ϕ , temperature T and specific humidity e_w at given pressure lev-
 623 els P . From these quantities, the virtual potential temperature, which takes
 624 into account the vertical pressure and humidity changes, can be calculated as:

$$T_{vp} = T (1 + [R_M - 1] e_w) \left(\frac{P_0}{P} \right)^{P_c(1-0.24e_w)}, \quad (17)$$

625 where $P_0 = 10^5$ Pa is the standard pressure, $P_c = 0.2854$ the Poisson coefficient
 626 for dry air and $R_M = 1.61$ is the ratio between the molecular masses of dry
 627 air and water. The vertical coordinates are calculated as:

$$z = \frac{\phi R_t}{g R_t - \phi}, \quad (18)$$

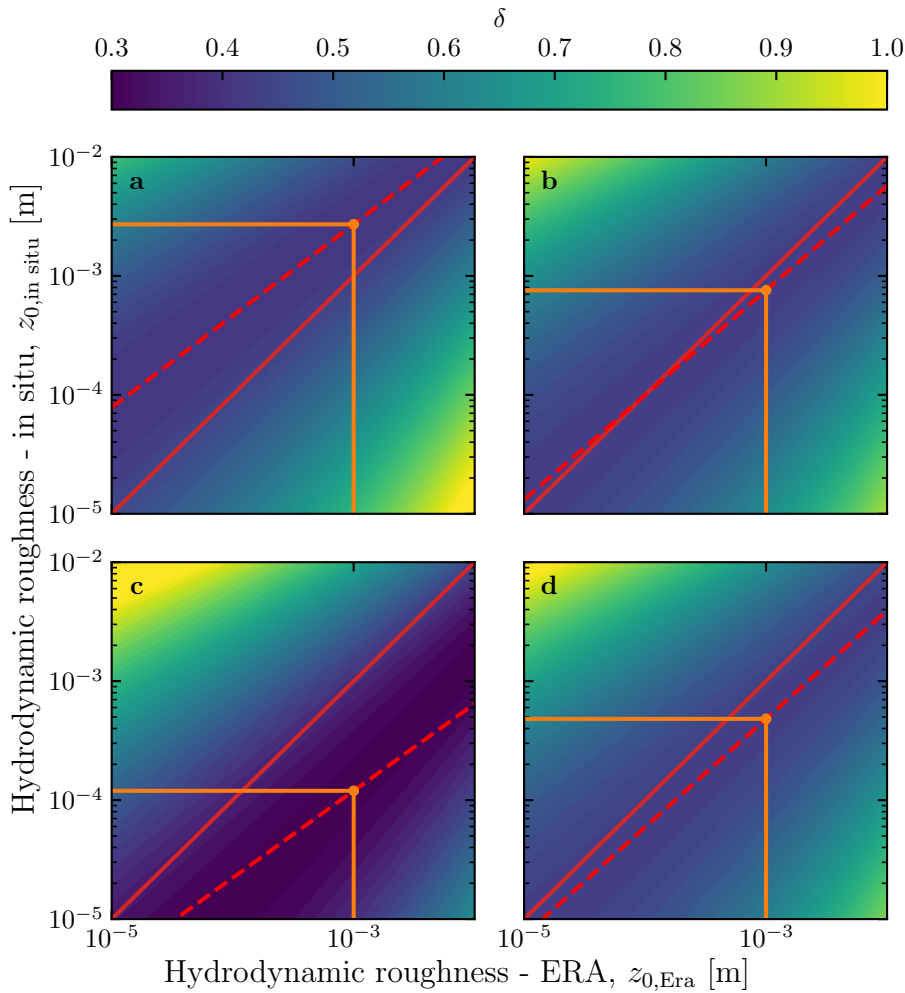


Fig. S3 Calibration of the hydrodynamic roughnesses. The metric δ defined in (16) is represented in colorscale as a function of the hydrodynamic roughnesses chosen for the Era5-Land and in situ datasets, for the Adamax (a), Deep Sea (b), Huab (c) and South Namib (d) Stations. The red dashed and plain lines shows the minima of δ and the identity line. The orange lines and dots highlight the chosen hydrodynamic roughnesses for the local datasets, by imposing $z_0,Era = 1$ mm, leading for each station to 2.7 mm, 0.76 mm, 0.12 mm and 0.48 mm, respectively.

where $R_t = 6356766$ m is the average Earth radius, and $g = 9.81$ m s⁻² the gravitational acceleration.

Example of obtained vertical profiles of the virtual potential temperature are shown in Fig. S9. On each of them, an average is computed below the ABL depth given by the Era5 dataset, and a linear function is fitted above.

Under the Boussinesq approximation, the temperature variations are assumed to induce most of those of the density, leading to $\Delta\rho/\rho \simeq \Delta T_{vp}/T_{vp}$.

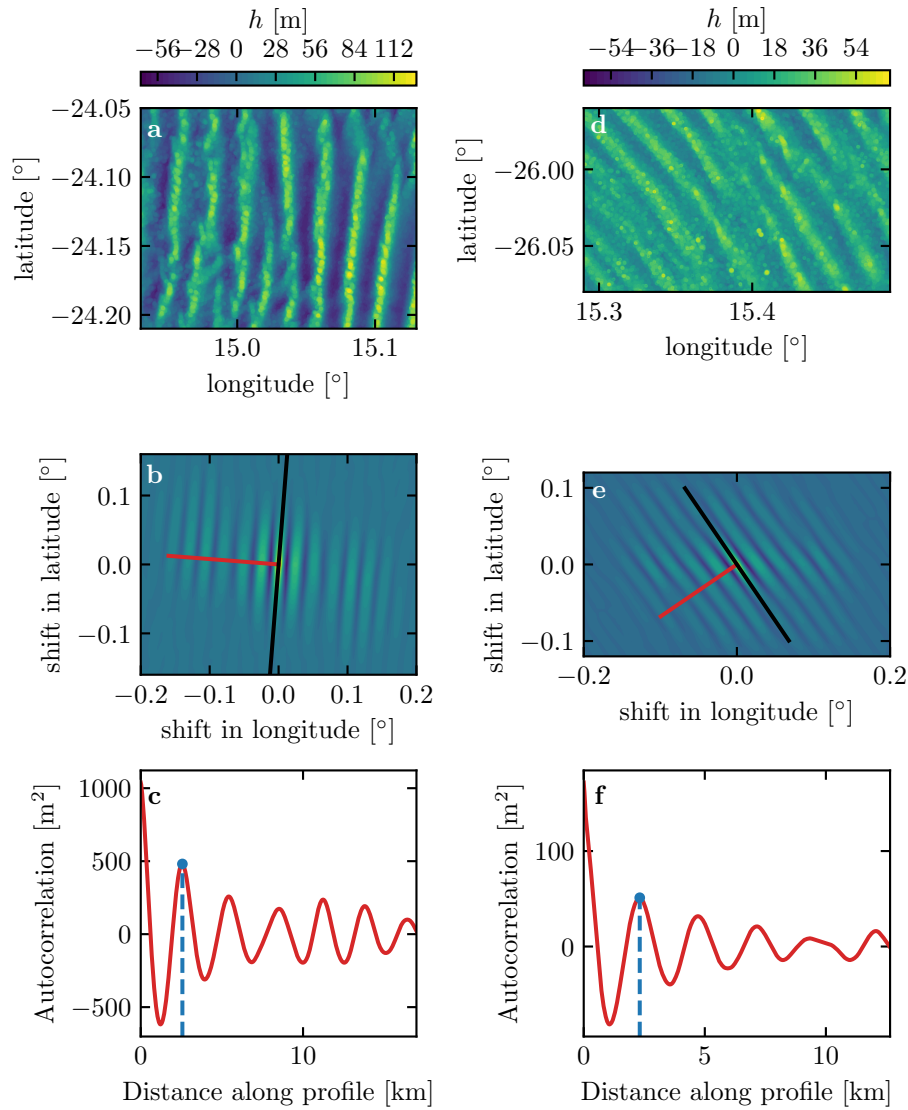


Fig. S4 Analysis of the DEMs of the Deep Sea (left column – **a**, **b**, **c**) and South Namib (right column – **d**, **e**, **f**) stations. **a–d**: Detrended topography (a second order polynomial is first fitted and then removed). **b–e**: autocorrelation matrix shown in colorscale. The black line shows the detected orientation, and the red line the profile along which the wavelength is calculated, shown in **c–f**. The blue lines and dots show the first peak of the autocorrelation profile, whose abscissa gives the characteristic wavelength of the dune pattern.

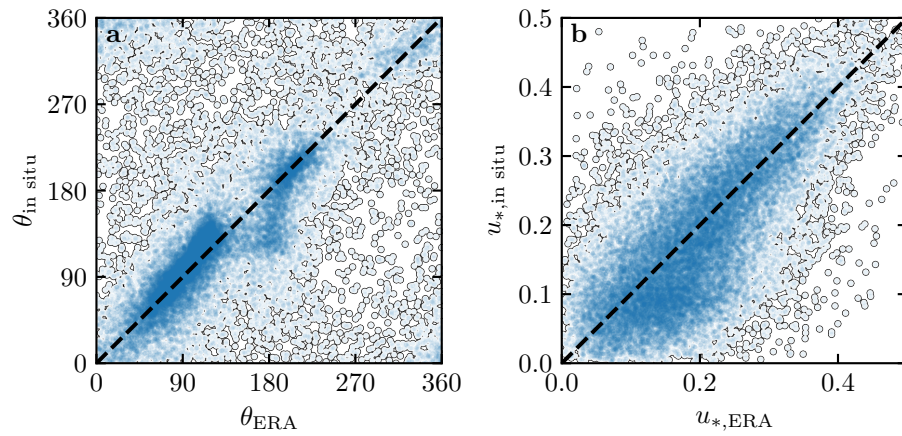


Fig. S5 Statistical agreement of the wind orientation (a) and velocity (b) between the Era5Land dataset and the local measurements for the Huab and Adamax stations. Note how the points are clustered around identity lines (dashed and black).

635 Here, $T_{\text{vp}}/T_{\text{vp}}$ is the relative virtual potential temperature jump at the capping,
636 directly measured on the vertical profiles.

637 Following Tritton (2012), the relative density jump at the capping layer

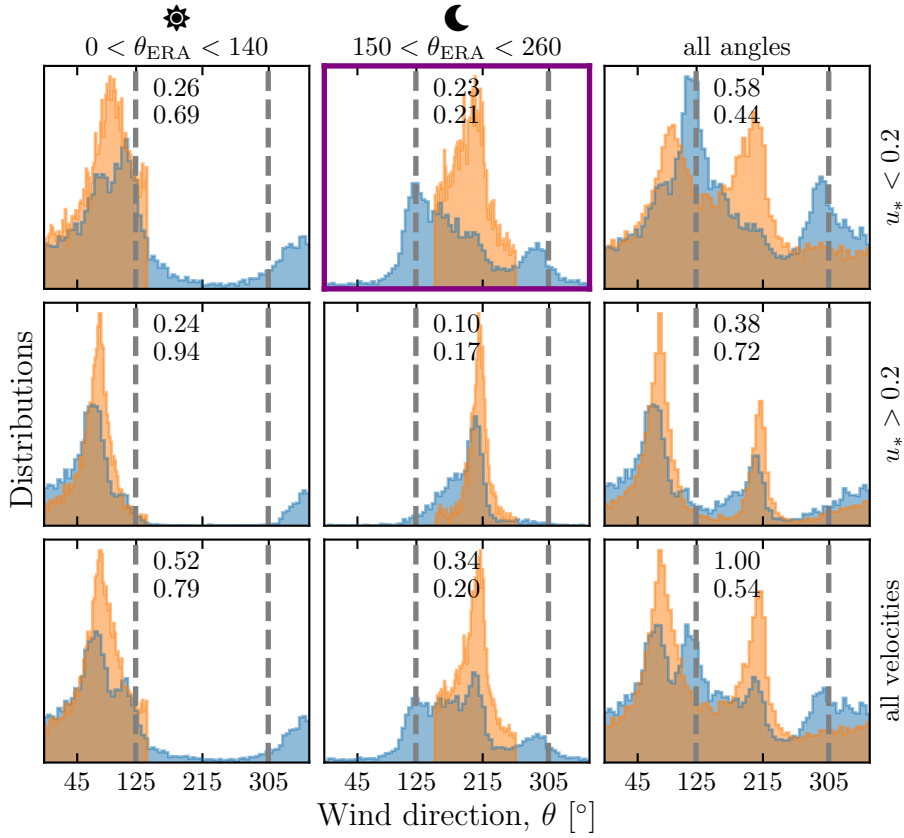


Fig. S6 Distributions of wind direction at the South Namib Station for the Era5Land climate reanalysis (orange) and the in situ measurements (blue). In each subplot, both distributions are plotted from the same time steps, selected with constraints on the wind direction (columns) and/or wind velocity (rows) in the Era5Land dataset. The gray vertical dashed lines indicate the dune orientation. The numbers at the top center give the percentage of time steps selected in each sub-range, as well as the percentage of them corresponding to the day (between 1000 UTC and 2200 UTC). The purple frame highlights the regime (small wind velocities, nocturnal summer wind) during which the wind data from both datasets differs. A similar figure can be obtained for the South Namib station (see Fig. 3).

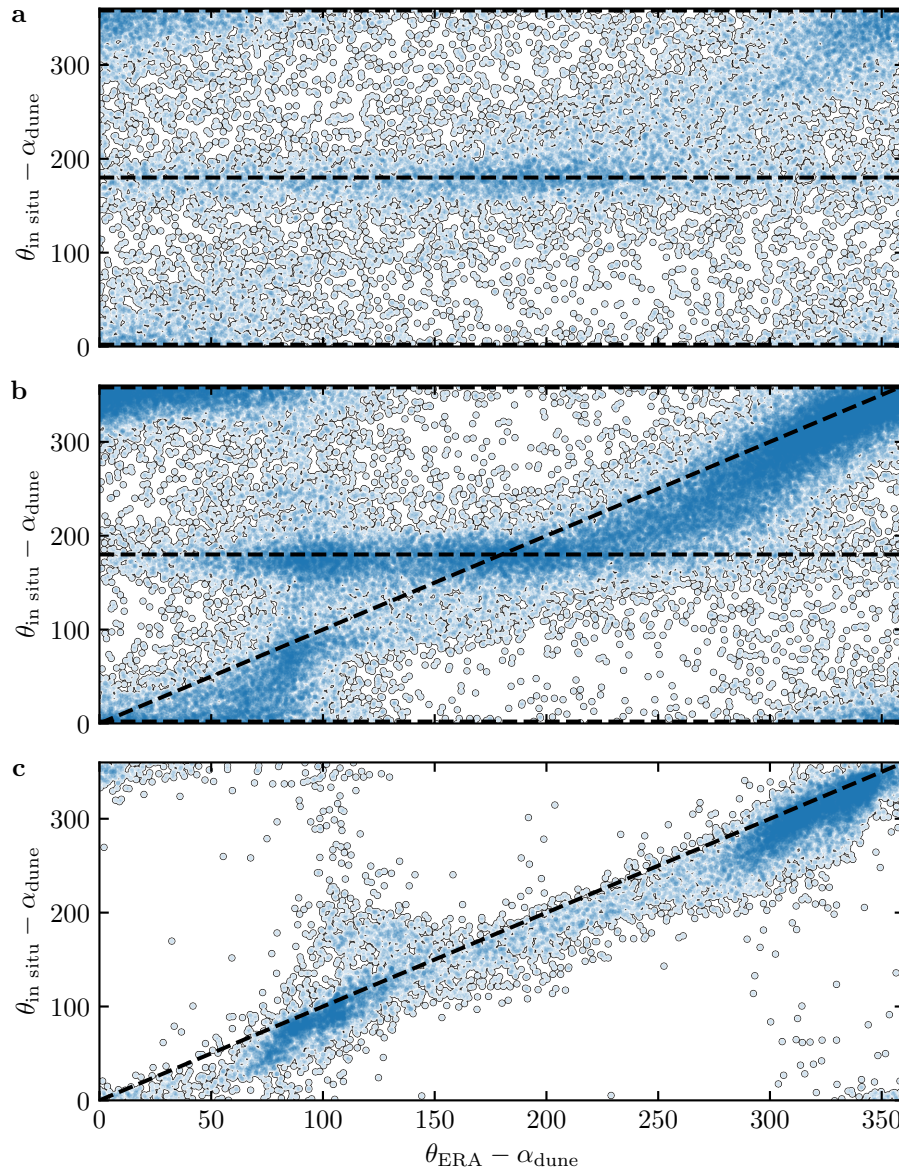


Fig. S7 Statistical comparison of the wind orientation between the Era5Land dataset and the local measurements for the South Namib and Deep Sea stations, for different velocity ranges. **a:** $u_{*,\text{ERA}} < 0.1 \text{ m s}^{-1}$. **b:** $0.1 < u_{*,\text{ERA}} \leq 0.25 \text{ m s}^{-1}$. **c:** $u_{*,\text{ERA}} \geq 0.25 \text{ m s}^{-1}$. Note that the measured dune orientations are subtracted to the wind orientation, which allows to plot both stations on the same graph. Black dashed lines indicate locally measured orientations aligned with the dune crests (here 0° , 180° and 360° – **a, b**), as well as the identity lines (**b, c**).

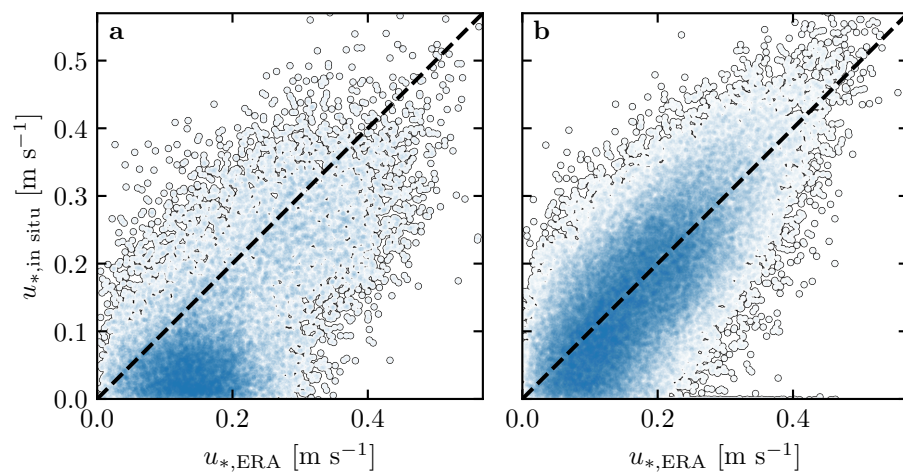


Fig. S8 Statistical comparison of the wind velocity between the Era5Land dataset and the local measurements for the South Namib and Deep Sea stations. **a:** Nocturnal summer easterly wind. **b:** Diurnal southerly wind. Black dashed lines are identity lines. The angle ranges used to select diurnal and nocturnal summer winds are those taken in Fig. 3 and Fig. S6.

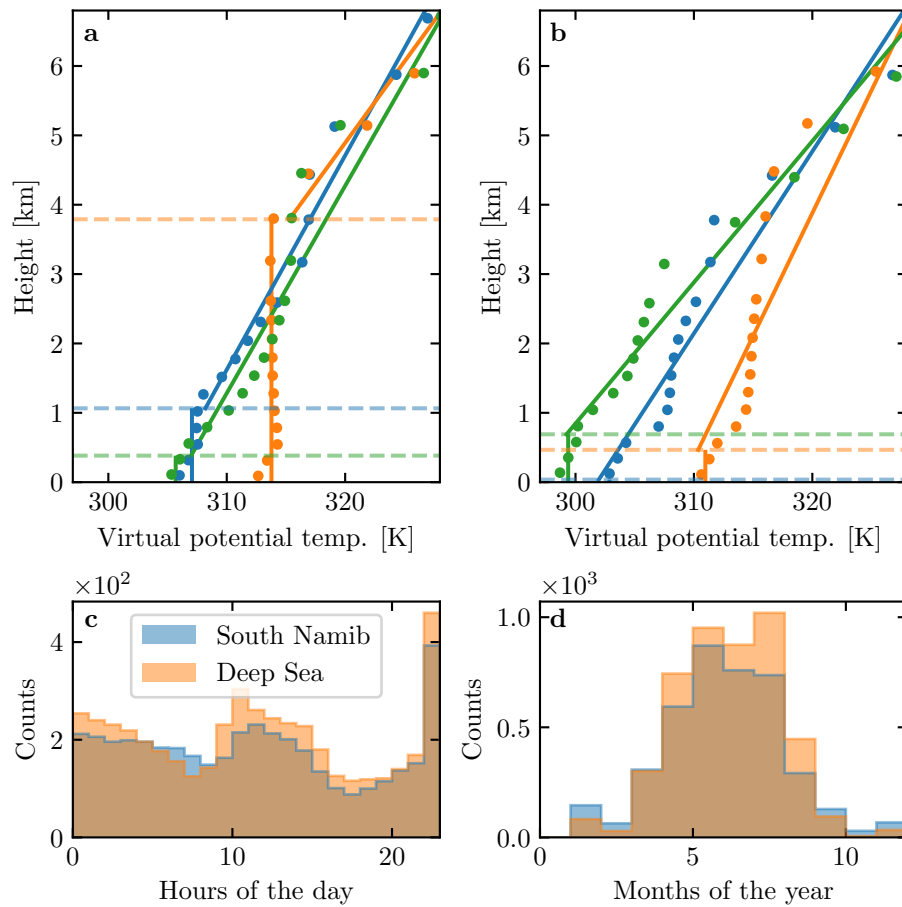


Fig. S9 **a:** Vertical profiles of the virtual potential temperature at 3 different time steps (blue - 29/11/2012 - 1100 UTC, orange - 21/03/2017 - 1200 UTC, green - 21/03/2017 - 2000 UTC) at the South Namib station. Dots: data from the ERA5 reanalysis. Transparent dashed lines: boundary layer height given by the ERA5 reanalysis, calculated from the bulk Richardson number (Seidel et al. 2012). Plain lines: vertical (boundary layer) and linear (free atmosphere) fits to estimate the quantities in Fig. S10. **b:** Examples of ill-processed vertical profiles at 3 different time steps (blue - 2/12/2013 - 2300 UTC, orange - 20/03/2017 - 0000 UTC, green - 14/07/2017 - 1400 UTC) at the South Namib station. **c:** Hourly distribution of ill-processed vertical profiles. **d:** Monthly distribution of ill-processed vertical profiles. These profiles are ill-processed because the temperature found at the boundary layer from the linear fit in the free-atm is smaller than the average one inside the boundary layer. This is an unstable situation, which does not allow to calculate the surface Froude number.

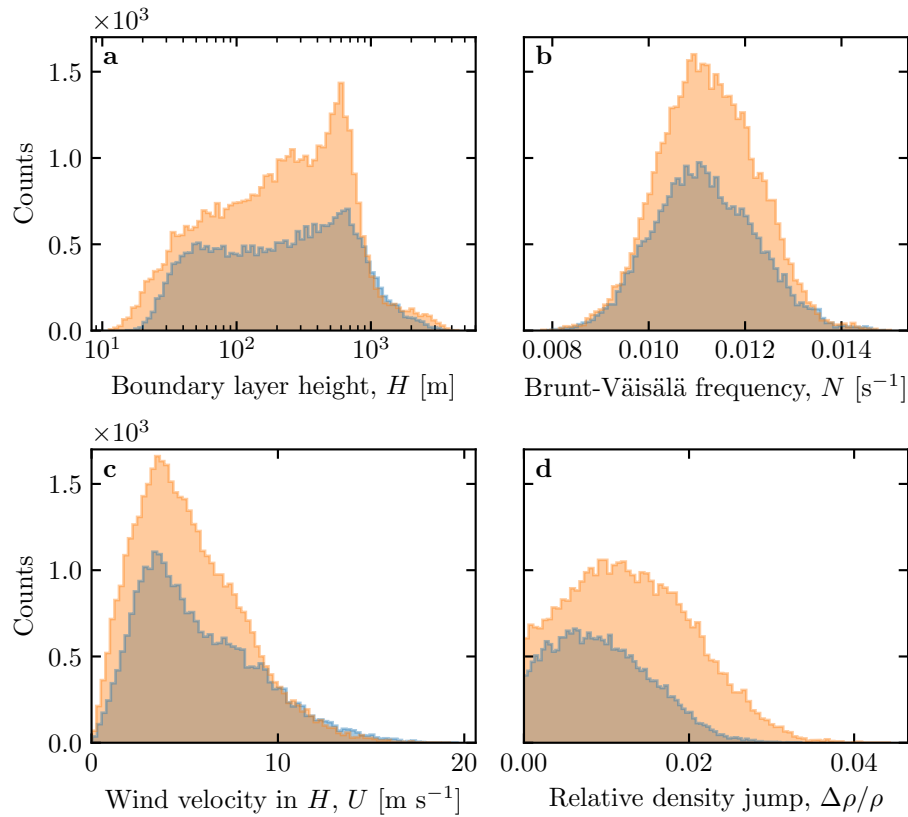


Fig. S10 Distributions of the meteorological parameters resulting from the processing of the Era5-Land data for the South Namib (blue) and the Deep Sea (orange) stations.

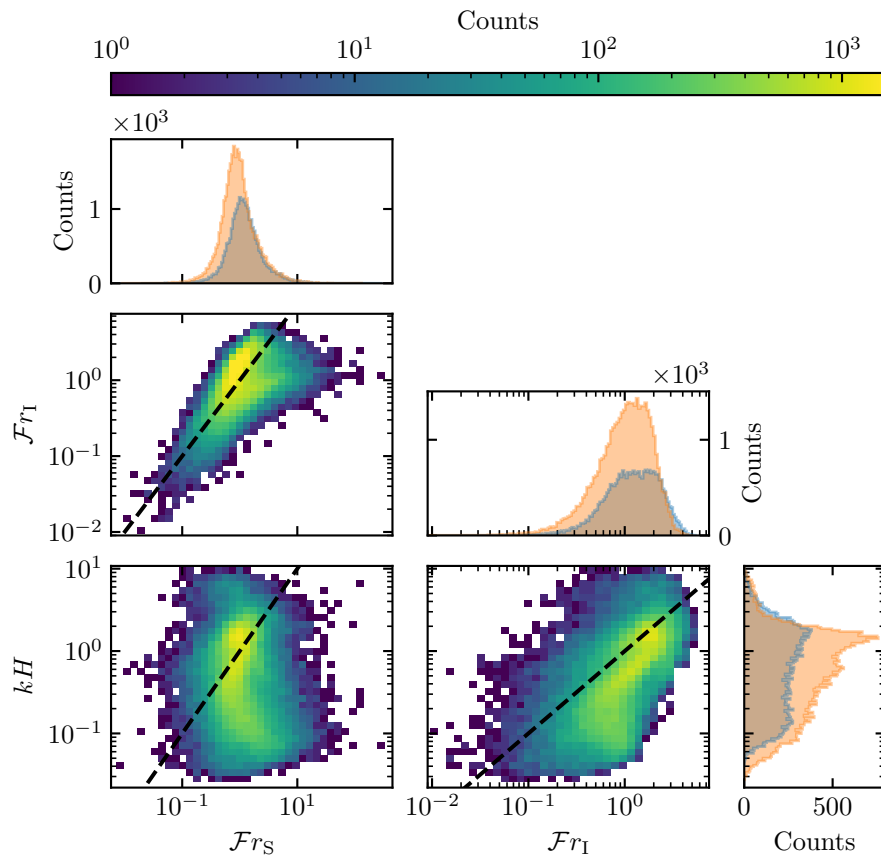


Fig. S11 Non-dimensional parameters distributions. For the marginal distributions, the orange correspond to the South Namib station, and the blue to the Deep Sea station.

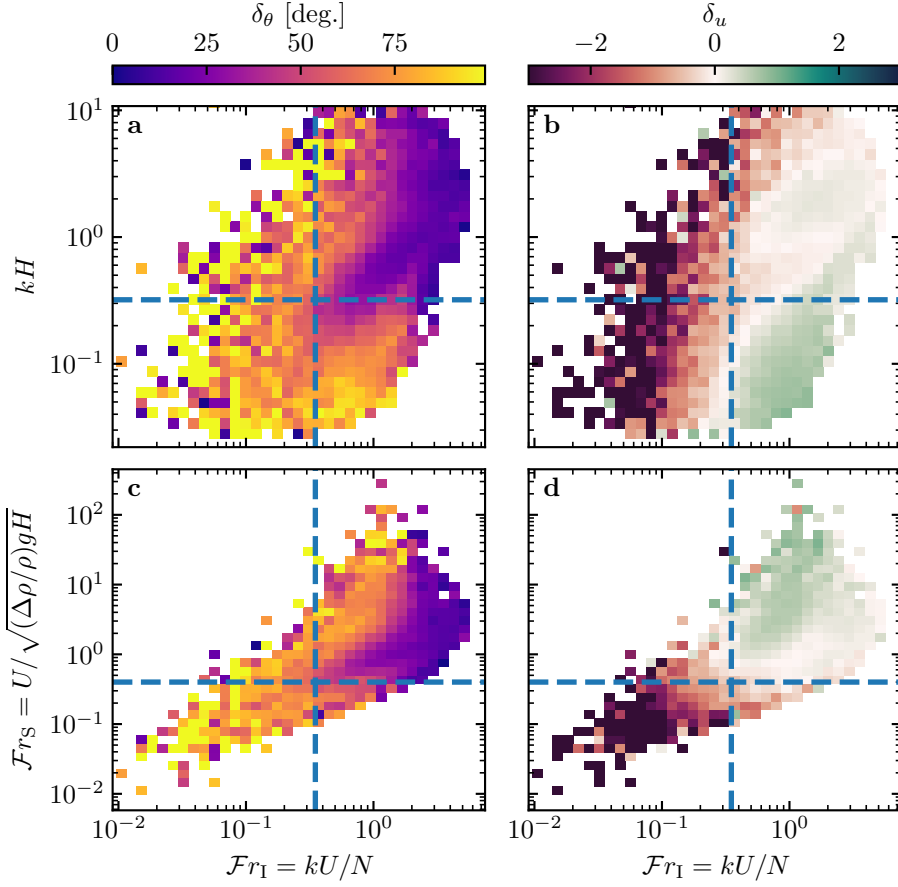


Fig. S12 Regime diagrams of the wind deviation δ_θ and relative attenuation/amplification δ_u in the spaces (\mathcal{F}_I, kH) and $(\mathcal{F}_I, \mathcal{F})$, containing the data from both the Deep Sea and South Namib stations. Blue dashed lines empirically delimit the different regimes. The point density in each bin of the diagrams is shown in Fig. S11. The regime diagrams in the space (\mathcal{F}, kH) are shown in Fig. 5 of the main article.

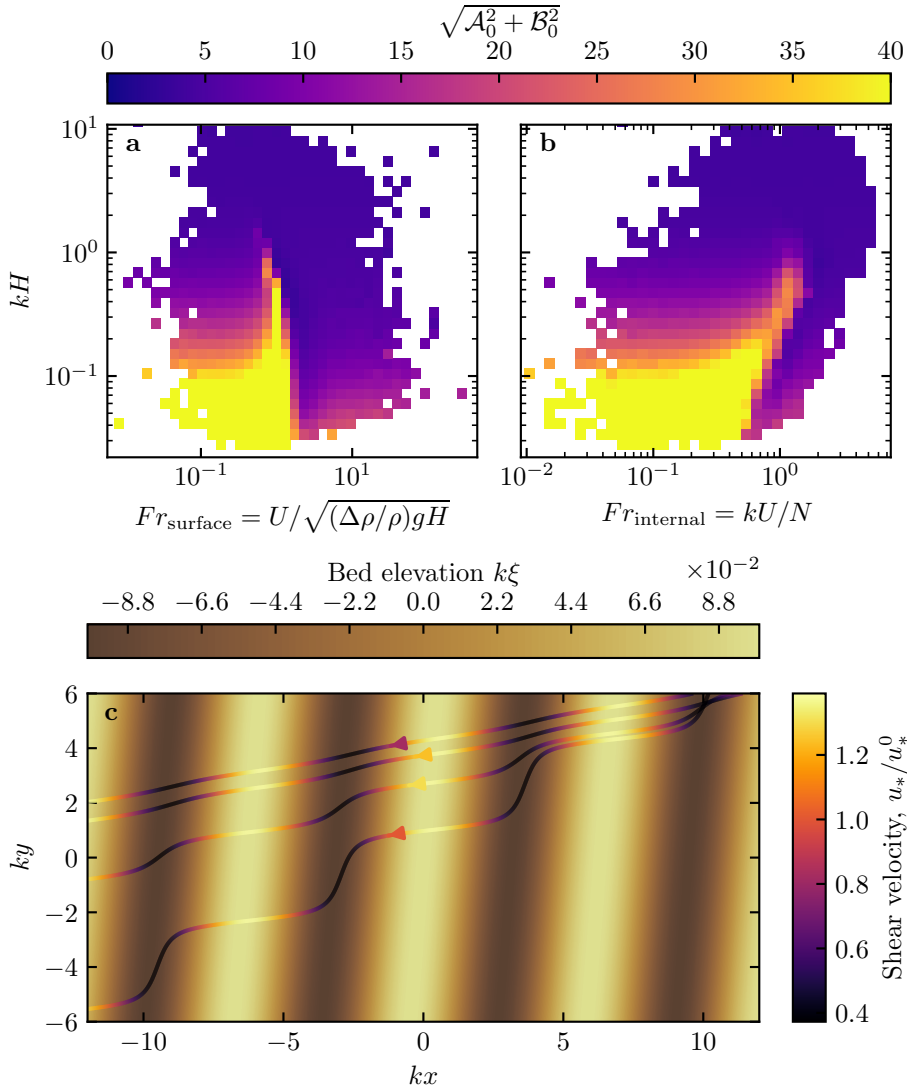


Fig. S13 Physical interpretation of the flow disturbance. (a) and (b) Magnitude of the disturbance induced by a sinusoidal topography calculated from the time series of the non-dimensional numbers presented in Figures 4 and 5 using the linear model of Andreotti et al. (2009). (c) Shear velocity streamlines represented in the case of the Deep Sea station, for increasing values of $\sqrt{\mathcal{A}_0^2 + \mathcal{B}_0^2}$. From the upper to the lower streamline, values of $(kH, Fr_{\text{surface}}, Fr_{\text{internal}}, \mathcal{A}_0, \mathcal{B}_0, \sqrt{\mathcal{A}_0^2 + \mathcal{B}_0^2})$ are $(1.9, 0.6, 1.5, 3.4, 1.0, 3.5)$, $(1.5, 0.3, 0.4, 4.8, 1.4, 5.0)$, $(0.1, 3.5, 1.0, 8.6, 0.1, 8.6)$, $(0.5, 0.05, 0.04, 9.6, 2.5, 9.9)$.